



Sensitivity of magnetic resonance elastography to extracellular matrix and cell motility in human prostate cancer cell line-derived xenograft models

Avan Kader^{a,b,c,*}, Joachim Snellings^a, Lisa C. Adams^{a,c}, Pablo Gottheil^d,
Dilyana B. Mangarova^a, Jennifer L. Heyl^a, Jan O. Kaufmann^{a,e}, Jana Moeckel^a,
Julia Brangsch^{a,c}, Timo A. Auer^{a,f}, Federico Collettini^{a,f}, Frank Sauer^d, Bernd Hamm^a,
Josef Käs^d, Ingolf Sack^a, Marcus R. Makowski^{a,c,g}, Jürgen Braun^a

^a Charité – Universitätsmedizin Berlin, corporate member of Freie Universität Berlin, Humboldt-Universität zu Berlin, and Berlin Institute of Health, Charitéplatz 1, 10117 Berlin, Germany

^b Department of Biology, Chemistry and Pharmacy, Institute of Biology, Freie Universität Berlin, Königin-Luise-Str. 1-3, 14195 Berlin, Germany

^c Technical University of Munich, Department of Diagnostic and Interventional Radiology, Ismaninger Str. 22, 81675 Munich, Germany

^d Peter Debye Institute for Soft Matter Physics, Leipzig University, Linnéstraße 5, 04103 Leipzig, Germany

^e Bundesanstalt für Materialforschung und -prüfung (BAM), Division 1.5 Protein Analysis, Richard-Willstätter-Str. 11, 12489 Berlin, Germany

^f Berlin Institute of Health (BIH), Berlin, Germany

^g King's College London, School of Biomedical Engineering and Imaging Sciences, St Thomas' Hospital, Westminster Bridge Road, London SE1 7EH, United Kingdom

ARTICLE INFO

Keywords:

Magnetic resonance elastography
Quantitative histology
Prostate cancer
Stiffness
Fluidity
Apparent diffusion coefficient
Collagen
Elastin
Nuclear shape

ABSTRACT

Prostate cancer (PCa) is a significant health problem in the male population of the Western world. Magnetic resonance elastography (MRE), an emerging medical imaging technique sensitive to mechanical properties of biological tissues, detects PCa based on abnormally high stiffness and viscosity values. Yet, the origin of these changes in tissue properties and how they correlate with histopathological markers and tumor aggressiveness are largely unknown, hindering the use of tumor biomechanical properties for establishing a noninvasive PCa staging system.

To infer the contributions of extracellular matrix (ECM) components and cell motility, we investigated fresh tissue specimens from two PCa xenograft mouse models, PC3 and LNCaP, using magnetic resonance elastography (MRE), diffusion-weighted imaging (DWI), quantitative histology, and nuclear shape analysis. Increased tumor stiffness and impaired water diffusion were observed to be associated with collagen and elastin accumulation and decreased cell motility. Overall, LNCaP, while more representative of clinical PCa than PC3, accumulated fewer ECM components, induced less restriction of water diffusion, and exhibited increased cell motility, resulting in overall softer and less viscous properties. Taken together, our results suggest that prostate tumor stiffness increases with ECM accumulation and cell adhesion - characteristics that influence critical biological processes of cancer development.

MRE paired with DWI provides a powerful set of imaging markers that can potentially predict prostate tumor development from benign masses to aggressive malignancies in patients.

Statement of significance: Xenograft models of human prostate tumor cell lines, allowing correlation of microstructure-sensitive biophysical imaging parameters with quantitative histological methods, can be investigated to identify hallmarks of cancer.

* Corresponding author at: Department of Radiology, Charité – Universitätsmedizin Berlin, Charitéplatz 1, 10117 Berlin, Germany.

E-mail addresses: avan.kader@charite.de (A. Kader), joachim.snellings@charite.de (J. Snellings), lisa.adams@tum.de (L.C. Adams), dilyana.mangarova@charite.de (D.B. Mangarova), jennifer.heyhl@charite.de (J.L. Heyl), jan-ole.kaufmann@charite.de (J.O. Kaufmann), jana.moeckel@charite.de (J. Moeckel), julia.brangsch@charite.de (J. Brangsch), timo-alexander.auer@charite.de (T.A. Auer), federico.collettini@charite.de (F. Collettini), sauer@physik.uni-leipzig.de (F. Sauer), bernd.hamm@charite.de (B. Hamm), jkaes@uni-leipzig.de (J. Käs), ingolf.sack@charite.de (I. Sack), marcus.makowski@tum.de (M.R. Makowski), juergen.braun@charite.de (J. Braun).

<https://doi.org/10.1016/j.bioadv.2024.213884>

Received 4 December 2023; Received in revised form 5 April 2024; Accepted 26 April 2024

Available online 29 April 2024

2772-9508/© 2024 The Authors. Published by Elsevier B.V. This is an open access article under the CC BY license (<http://creativecommons.org/licenses/by/4.0/>).

1. Introduction

Prostate cancer (PCa) is one of the most diagnosed tumors in men in the Western world, usually detected at a late stage, when mortality is high [1]. PCa is a heterogeneous disease, ranging from small, indolent, low-grade abnormalities to large, aggressive, life-threatening cancers, and is largely asymptomatic in its early stages. Manual rectal examination of prostatic stiffness and prostate-specific antigen (PSA) blood tests are commonly used to screen for PCa, while invasive transperineal prostate biopsy continues to be the gold standard for staging. Early detection and noninvasive characterization of PCa remain challenging because ultrasound and magnetic resonance imaging (MRI) rely on nonquantitative and nonspecific imaging markers, whose association with tissue architecture at the microscopic level is largely unknown. In addition, although multiparametric magnetic resonance imaging (mpMRI) can noninvasively characterize the structure, proliferation characteristics, and water diffusion in suspicious lesions, it is reader-dependent and can lead to false-positive or false-negative results.

There is increasing evidence that the extracellular matrix (ECM) plays a critical role in tumor progression [2], making the ECM a favorable target for cancer diagnosis and therapy. The ECM is composed of a complex network of macromolecules [2] with collagen (types I, III, V, and others), elastin, and fibronectin as major components. Alterations in the ECM can drive cancer progression through mechanoadaptive cell response mechanisms [3]. This dynamic interplay is vital for tissue and organ physiology, as well as for cancer development. In tumorigenic conditions, the matrix undergoes significant dysregulation, exhibiting both tumor-promoting and antitumor effects [4–7]. Although prostate cancer is not traditionally considered a stromal-dense cancer like breast or pancreatic cancer, emerging evidence suggests that ECM alterations are a key feature of PCa progression, particularly in the development of metastatic and treatment-resistant disease [8].

PCa has a collagen-rich stroma in the tumor microenvironment, resulting in overall higher tumor stiffness [9], which promotes all hallmarks of cancer [10], including activation of invasion and metastatic spread [11]. An increase in collagen type 1 synthesis in activated peri-acinar fibroblasts was observed, which was associated with the stiffening of the tumor tissue [12]. This suggests that the increase in collagen content in prostate tissue is associated with early stages of PCa development. Patient data also show a strong correlation between collagen-mediated tumor stiffness and tumor development and aggressiveness. Recently, quantification of ECM elements in prostate adenocarcinomas of different Gleason scores revealed an increase in collagen fibers in the tumor area compared to the non-tumor area [13]. Tissue stiffness and viscosity can be determined with high accuracy using magnetic resonance elastography (MRE) [14]. Technical improvements in MRE have enabled the detection and biomechanical characterization of small tumor lesions within short scan times, and MRE has been successfully applied to a wide range of cancers in different body regions and organs including the brain [15], liver [16], and pancreas [17]. In PCa, MRE integrated into standard clinical MRI protocols has been shown to add diagnostic value [18]. MRE studies of PCa specimens have used excised human tissue to investigate the relationship between coarse-grained biomechanical properties and histology [19]. In addition to MRE-measured stiffness, tissue fluidity has recently been introduced as a mechanical parameter that is related to the ratio of loss to storage properties providing additional information for tumor characterization [14,20,21]. It has been argued that the fluidity of soft solid tissues reflects the ability of cells to change position and thus relates to the state of jamming and unjamming of cancer cells [22]. Specifically, stiff and heterogeneous tumors have been shown to contain soft and motile cells [23] with elongated cell and nucleus shapes [24] resulting in higher fluid properties than benign tumors [22].

In addition to established tumor cell lines such as PC3 and LNCaP, researchers have also used CDX and PDX models to study prostate cancer [25]. CDX models involve the implantation of cancer cell lines into

immunocompromised mice, providing a controlled system for studying tumor behavior and drug response [25]. PDX models, on the other hand, involve transplantation of patient-derived tumor tissue directly into mice, providing a more representative model of human prostate cancer [25]. While both approaches have their advantages and limitations, the current study used cell line-derived xenografts to investigate the biophysical properties of prostate tumors. Human prostate cancer xenograft mouse models have turned out to be suitable systems to study the interactions between tumor cells and their microenvironment [26]. Two cell lines, PC3 [27] and LNCaP [28], which were originally derived from bone and lymph node metastases, are available to grow tumors with different biological characteristics. PC3-derived tumors are often used as a model to study advanced prostate cancer, as they are characterized by increased expression of growth factors and cytokines, mutations in tumor suppressor genes, high metastatic potential, androgen insensitivity, and resistance to chemotherapy [29]. LNCaP-based tumors provide the most clinically relevant tissue culture of androgen-dependent prostate cancer with elevated prostate-specific antigen (PSA), allowing the study of treatment responses to anti-androgen therapy [29]. However, there is only a limited amount of data available on the biomechanical properties of human prostate cancer xenograft mouse models [30].

The aim of this study is to investigate the human PCa cell lines PC3 and LNCaP in an ectopic xenograft model in immunocompromised (SCID) mice to correlate the parameters of stiffness, solid tissue fluidity, and water mobility measured by MRE and diffusion-weighted imaging (DWI) with histologic cancer features of ECM proliferation and cell motility. The results of these experiments will allow us to determine whether noninvasive biophysical imaging techniques have the potential to predict cancer progression in the clinical setting.

2. Methods

2.1. Cell culture

PC3 cells and LNCaP cells were obtained from ATCC® CRL-1435™ (Manassas, USA) and grown in Roswell Park Memorial Institute (RPMI) 1640 medium (Gibco™, Thermo Fischer Scientific, Waltham, USA) supplemented with 10 % fetal calf serum (FCS) (Gibco™, Thermo Fischer Scientific, Waltham, USA). Cells were cultured in 150 cm³ tissue culture flasks at 37 °C and 5 % CO₂ until they were approximately 75–80 % confluent. The cells were then washed with phosphate-buffered saline (PBS) (Gibco™, Thermo Fischer Scientific, Waltham, USA), trypsinized, and resuspended in 1 ml of RPMI medium. Cells were counted using 0.4 % trypan blue solution (Gibco™, Thermo Fischer Scientific, Waltham, USA).

2.2. Xenograft mouse model and study design

Experiments were conducted in accordance with the local guidelines and regulations for the implementation of the Animal Welfare Act and the regulations of the Federation of Laboratory Animal Science Associations (FELASA). The animal experiments were approved by the supervisory authority of the Berlin State Office for Health and Social Affairs (LAGESo) (G0094/19). The animals were housed in a controlled environment with a 12-h light/dark cycle, ad libitum access to food and water, and enrichment materials such as nesting material and tubes. Eight-week-old male SCID mice (CB17/Icr-Prkdcscid/IcrIcoCrI, *n* = 20) were purchased from Charles River Laboratories (Sulzfeld, Germany). The mice were randomly divided into two groups (*n* = 10). Mice were anesthetized by intraperitoneal injection of medetomidine (500 µg/kg), midazolam (5 mg/kg), and fentanyl (50 µg/kg).

The cell suspension containing 2×10^6 PC3 cells (group 1) or LNCaP cells (group 2) was injected subcutaneously into the right scapular region.

Anesthesia was subsequently antagonized with atipamezole (750 µg/

kg), flumazenil (0.5 mg/kg), and naloxone (1200 µg/kg). Once a tumor size of approximately 1000 mm³ was reached, as measured with a caliper, the mice were anesthetized again and then euthanized. The subcutaneous xenograft mouse model allows good monitoring of tumor growth and reduces stress on the animal. The experimental steps are illustrated in Fig. 1A.

2.3. Sample preparation

PC3 and LNCaP tumors were surgically separated from the surrounding tissue. Half of the tumor was used for tabletop MRE and the other half for histology. It took about 3–5 min from collection to the MRE examination. The tumor specimen for MRE was prepared by cutting a cylindrical tissue sample measuring approximately 7.5 mm in diameter. The cylindrical sample was carefully transferred into a custom-made glass sample tube (length: 200 mm, outer diameter: 9 mm, inner diameter: 7 mm) (Fig. 1B, C). After sealing with plastic plugs to prevent drying, the sample tube was connected to the piezo actuator and inserted into the magnet of the scanner (Fig. 1D).

2.4. Ex vivo multifrequency MRE

As described in detail in [31], a tabletop MRI scanner (Pure Devices GmbH, Würzburg, Germany) with a 0.5-T permanent magnet with a 10-mm bore was customized for MRE by addition of a four-channel external gradient amplifier (DC 600, Pure Devices GmbH, Würzburg, Germany) and an integrated MRI system-controlled piezoelectric driver (PAHL 60/20, Piezosystem Jena GmbH, Jena, Germany). To account for inherent differences in the stiffness of the two tumor types used in our experiments, we sequentially induced shear waves with frequencies f of 2400, 2750, 3250, 3500, and 4000 Hz for stiff PC3 tumors and 600, 800, 1020, 1180, 1340, 1500, 1660, 1820, 2000, 2140, 2400, 2800, 3000, 3160, and 3500 Hz from the wall of the sample tube for softer LNCaP tumors. The resulting concentric shear waves propagated towards the center of the tissue sample. Wave images were acquired using a spin-echo-based MRE sequence [31] with trapezoidal bipolar motion-encoding

gradients (MEGs) of 0.2 T/m amplitude, polarized along the cylinder axis (thru-plane) and synchronized to the vibration frequency f . A MEG encoding time of 20 ms was set for all frequencies, resulting in a variable number of MEG cycles ranging from 12 to 80 for frequencies from $f = 600$ to 4000. Other acquisition parameters were: repetition time (TR): 350 ms, echo time (TE): 30 ms, field of view (FoV): 9.6×9.6 mm², matrix size: 64×64 , in-plane resolution: 150×150 µm², and slice thickness: 3.0 mm. Total acquisition time for all vibration frequencies, each of which was sampled with four wave dynamics, was approximately 8 min per sample for PC3 and 23 min for LNCaP tumors.

According to [32], the shear wave speed (c in m/s) and the penetration rate (a in m/s) as markers of stiffness and attenuation were calculated by fitting the analytical solution of shear waves in a z-infinite cylinder from the complex-valued wave images after phase unwrapping and temporal Fourier transform. Subsequently, we fitted the rheological spring-pot model to c and a in order to derive frequency-independent stiffness values μ (in Pa) and the dimensionless power-law exponent α . The spring-pot model showed the best fit to the experimental data of both tumors compared with the Kelvin-Voigt and Maxwell models and is characterized by a monotonic increase in both storage and loss moduli with frequency [33]. Using the material density ρ_0 (set to 1 kg/l in this study), we can express c and a as [20]:

$$c(\omega) = \sqrt{\frac{\mu^{1-\alpha} \eta^\alpha \omega^\alpha}{\rho_0}} \frac{1}{\cos\left(\frac{\pi}{4}\alpha\right)} \quad (1)$$

$$a(\omega) = \sqrt{\frac{\mu^{1-\alpha} \eta^\alpha \omega^\alpha}{\rho_0}} \frac{1}{2\pi \sin\left(\frac{\pi}{4}\alpha\right)} \quad (2)$$

with independent variables μ (in Pa) and α . Intrinsic viscosity η is not independent and was set to 1 Pa·s in this study. Power-law parameter α has two limits: 0 for purely elastic-solid behavior and 1 for purely viscous-fluid properties. This is similar to the loss angle φ of the complex shear modulus $G^* = |G^*| \exp i\varphi = G' + iG''$ which indicates solid-elastic

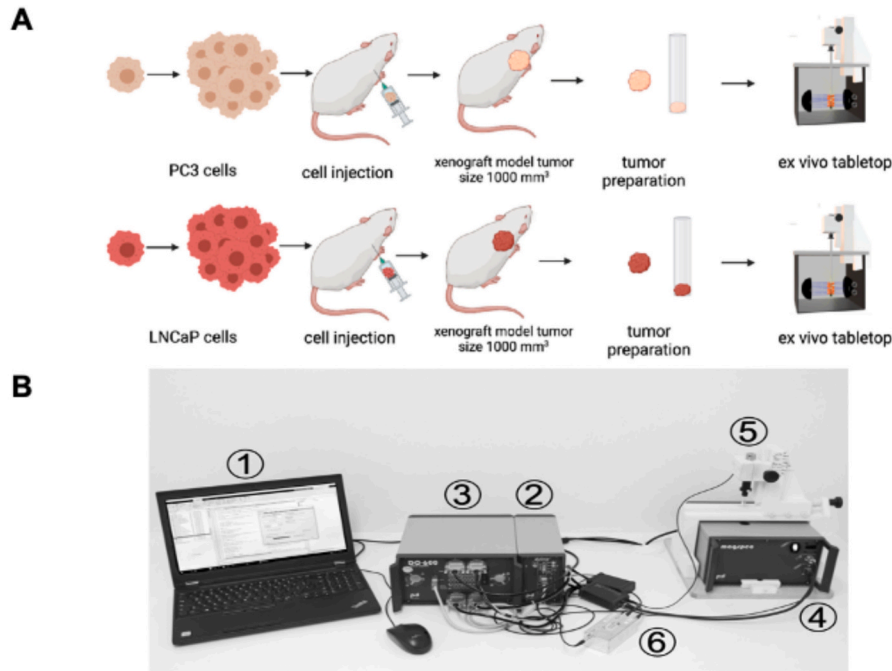


Fig. 1. Experimental design and preparation of PC3 and LNCaP tumor types for multifrequency MRE in a compact tabletop MRI scanner. (A) PC3 and LNCaP cancer cells are cultured and then injected into the right scapula area of a SCID mouse. Once a tumor size of approximately 1000 mm³ has been reached, the mouse is euthanized, and the tumor prepared for ex vivo tabletop MRE in a glass tube. (B) Customized MRE system: (1) control computer, (2) electronics cabinet, (3) external gradient amplifier, (4) 0.5-Tesla magnet, (5) piezo-based actuator mounted on the sample tube (see also this figure), and (6) preamplifier.

properties at 0 and increases towards fluid tissue properties with a maximum value of $\pi/2$:

$$\varphi(\omega) = \arctan \frac{G'(\omega)}{G''(\omega)} = 2 \arctan \frac{c(\omega)}{2\pi a(\omega)} \quad (3)$$

A frequency independent estimate of tissue fluidity can be obtained from the power-law coefficient of the spring-pot model [34]:

$$\varphi = \frac{\pi}{2} \alpha. \quad (4)$$

Importantly, the notion of φ as a measure of *tissue fluidity* differs from that of liquids, which have higher fluidity at lower viscosity values while φ increases with G'' . This is because MRE is sensitive to the motility of particles and structures that transmit shear forces but not liquid behavior. Therefore, viscosity in MRE is only attainable through viscoelastic modeling in combination with a shear modulus.

Diffusion-weighted imaging (DWI) was performed with a customized spin-echo sequence [35] using seven b-values (0, 27.8, 111.1, 250.0, 444.4, 694.4, and 1000.0 s/mm²). A single 3-mm slice with an in-plane resolution of 600 μ m was acquired with a TR of 1 s and a TE of 8 ms. Total acquisition time for DWI was approximately 2 min.

2.5. Histological stains

Frozen tumor specimens were cut into 10 μ m thick serial sections at -20°C . Samples were fixed in acetone (99 %, Fisher Scientific, Hampton, United States) for 6 min at -20°C . *Elastica* van Gieson (EvG) (Elastin Stain (Miller), VWR Chemicals, United States;) staining was performed to detect elastic fibers, and Picrosirius red (PSR) (Morphisto GmbH, Germany) staining was performed to detect collagen. Visualization and analysis were performed with a light microscope (Keyence BZ-X800, Keyence Ltd. HQ & Laboratories, Osaka, Japan). Three randomly representative areas were analyzed per sample (PC3 $n = 10$; LNCaP $n = 10$).

2.6. Quantitative measurement of elastin

Tumor samples were initially weighed, lyophilized, and reweighed ($n = 6$ per group). The Fastin™ Elastin Assay (biocolor, United Kingdom), which includes all reagents, was used for this analysis. The dry tissue was placed in a microcentrifuge tube, and 750 μ l of 0.25 M oxalic acid was added. The tubes were then stored at 100°C for 60 min. After cooling to room temperature, the tubes were centrifuged at 13,000 G for 10 min. An equal volume of elastin precipitation reagent was added to each sample, vortexed briefly, and allowed to stand for 15 min. Blank values and standards were included. The tubes were then centrifuged for 10 min, and liquid was completely removed from each tube. Next, 1 ml of dye reagent was added to each tube and mixed. The samples were then shaken in the shaker for 90 min, centrifuged at 13,000 rpm for 10 min, and then vortex after addition of 250 μ l of the dye dissociation reagent. After 10 min, vortex mixing was repeated. 100 μ l of the extract was transferred to a 96-well flat-bottom MicroWell™ plate. Absorbance was then measured using a photometer (PowerWave™ HT Microplate Spectrophotometer, USA) and the values were quantified as RFU. The results were statistically analyzed ($n = 6$).

2.7. Quantitative measurement of collagen

The QuickZyme Biosciences Collagen Assay (QuickZyme Biosciences B.V., Netherlands), which contains all reagents, was used for collagen analysis in tumor tissue. For preparation, dry tumor samples ($n = 6$ per group) were treated with 6 M HCl and incubated at 95°C in a thermoblock for 20 h. After incubation, the tubes were cooled to room temperature and centrifuged at 13,000 rpm for 10 min. 35 μ l of the supernatant was used for further analysis. The hydrolyzed samples were diluted with deionized water: 1 volume of sample was added to 0.5

volume of deionized water (2:1). Standard controls were included. Assay buffer was then added and the samples were incubated for 20 min at room temperature with shaking. A sufficient amount of detection reagent was then prepared by mixing detection reagents A and B (2:3). 75 μ l of the detection reagent was added to each well. The plate was covered and shaken, followed by incubation for 60 min at 60°C . The samples were then allowed to cool down to room temperature by placing them on ice for 5 min. Finally, the plate was shaken again, and the absorbance was measured at 570 nm using a photometer (PowerWave™ HT Microplate Spectrophotometer, USA) and the values were quantified as RFU. Statistical tests were performed on the results ($n = 6$).

2.8. Quantification of cell nucleus shape and nucleus area

The determination of cell nuclear shape as a measure of cell motility is described in detail in [24]. The main steps of H&E staining analysis of explanted PC3 ($n = 10$) and LNCaP ($n = 10$) xenograft tumors are: (i) color separation into eosin and hematoxylin, (ii) denoising of the hematoxylin channel, (iii) segmentation of the hematoxylin channel, and (iv) cell approximation. Three areas were selected and analyzed for each tumor (area $0.97 \times 0.73 \text{ mm}^2$). 9699 ± 4160 cells were measured. Nuclear elongation was quantified as the aspect ratio (AR) of the long and short axes of ellipses with the same standardized second central moments as the underlying nuclear segments segmented in the image data. The areas of elliptical nuclei ($\text{AR} \neq 1$) were calculated using the determined long and short axes, and the areas of round nuclei ($\text{AR} = 1$) were calculated using the radius. Nuclei density area was quantified from the total number of nuclei per area [36]. The area is defined as the area covered by confluent (high density) cell regions. The methodology was adapted from Gottheil et al. [36] to which we refer for further technical details and algorithms.

2.9. Statistical analysis

2.9.1. Ex vivo multifrequency MRE and histological results

Values are reported as median \pm median absolute deviation (MAD). We calculated the MAD by taking the median of the absolute value of the differences of the data from their median, i.e., $\text{median}(\|x - \text{median}(x)\|)$, where x is a data vector. Lilliefors tests were used to analyze the data for normal distribution. A two-tailed Wilcoxon rank sum test (Matlab Statistics and Machine Learning toolbox R2020b, The MathWorks, Inc., Natick, Massachusetts, USA) was used to compare continuous distributions with equal medians. A p -value < 0.05 was considered to indicate a statistically significant difference.

2.9.2. Nucleus shape analysis

Pearson's correlation coefficient (PCC) was used to calculate the relationship between nucleus shape and cell shape of tumor cells using H&E-stained explants of the PC3 and LNCaP xenograft tumor lines. Coefficients range from 0 for no correlation to 1 for perfect correlation. The MATLAB built-in `corrcoef` function (Matlab Statistics and Machine Learning toolbox R2020b, The MathWorks, Inc., Natick, Massachusetts, USA) was used, correlations were considered significant at p -values < 0.05 .

2.10. Correlation analysis

Because the Lilliefors test revealed nonnormal distribution, Spearman's rank correlations were calculated to test for associations between biophysical and histological tissue parameters of PC3 and LNCaP tumors (Matlab Statistics and Machine Learning toolbox R2020b, The MathWorks, Inc., Natick, Massachusetts, USA). Spearman's rank correlation can range from +1 to -1 , where +1 indicates a perfect association between ranks, 0 indicates no association between ranks, and -1 indicates a perfect negative association between ranks. Correlations were considered significant at p -values < 0.05 .

3. Results

All mice ($n = 20$) developed tumors. The tumors reached their target size 44–61 days after cell implantation. However, one mouse was euthanized prematurely due to poor body condition. To maintain a consistent sample size, this mouse was replaced with another.

3.1. MRI

The two tumor types investigated showed fundamental differences in stiffness-related shear wavelength and viscosity-related shear wave damping, as illustrated by the wave images presented in Fig. 2A. As shown in Fig. 3 for the range of overlapping vibration frequencies, PC3 tumor samples exhibited significantly higher c and a values than LNCaP, indicating higher stiffness and lower damping values at 2400 Hz (5.96 ± 0.54 vs. 2.81 ± 0.27 m/s, $p < 0.0005$; 1.70 ± 0.35 vs. 0.91 ± 0.12 m/s, $p < 0.0005$) and 3500 Hz (5.46 ± 0.39 vs. 3.07 ± 0.21 m/s, $p < 0.0005$; 1.48 ± 0.24 vs. 0.86 ± 0.15 m/s, $p < 0.005$). Table 1 summarizes all frequency-dependent values of c and a for all samples tested.

Fig. 4 illustrates the results of fitting the rheological spring-pot model. Consistent with the findings for c and a , μ (Fig. 4A) and α (Fig. 4B) were significantly higher in PC3 compared to LNCaP tumor samples (28.92 ± 13.16 kPa vs. 3.11 ± 1.15 kPa, $p < 0.0005$; 0.61 ± 0.05 vs. 0.51 ± 0.06 , $p < 0.05$). At a frequency of 3000 Hz (center of frequency range), wave velocities of 2.96 ± 0.13 and 5.23 ± 0.61 m/s and penetration rates of 1.10 ± 0.13 and 1.51 ± 0.34 m/s were calculated for LNCaP and PC3 tumors, respectively, based on spring-pot parameters μ and α . Tissue fluidity ϕ calculated from α for the two xenograft tumor types using Eq. 3 is shown in Fig. 4C. Although stiffer, PC3-derived tumors showed significantly higher ϕ values than LNCaP

tumors (0.96 ± 0.09 vs. 0.81 ± 0.10 , $p < 0.05$). All rheological MRE parameters are summarized in Table 2.

ADC was determined as an additional quantitative MRI parameter. LNCaP exhibited significantly higher ADC values, indicating increased water mobility compared with PC3 tumor specimens (0.86 ± 0.06 vs. $0.55 \pm 0.03 \times 10^{-3}$ mm²/s, $p < 0.0005$). The numerical results of this analysis are summarized in Table 3.

3.2. Quantitative analysis of ECM components

PC3 tumors contained more elastin fibers and collagen fibers than LNCaP tumors. EvG staining showed an average of 3.6 ± 0.8 % in PC3 and 2.1 ± 0.6 % in LNCaP tumors for elastin, corresponding to a 71 % increase in elastin in PC3 compared with LNCaP. The difference was significant, $p < 0.01$. A similar effect was observed for collagen in PSR-stained samples: PC3 tumors 3.5 ± 0.5 % and LNCaP tumors 2.2 ± 1.0 %, corresponding to a 59 % increase in collagen ($p < 0.01$, Fig. 5A).

Elastin levels were 1.49 ± 0.35 relative fluorescence unit (RFU) and for LNCaP tumors were 1.12 ± 0.17 RFU (corresponding to a 33 % higher elastin level in PC3 increase in elastin ($p < 0.01$, Fig. 5B)). The collagen level for PC3 was 0.33 ± 0.06 RFU and 0.2 ± 0.03 RFU for LNCaP, indicating a significantly higher collagen level for PC3 compared to LNCaP ($p < 0.001$, Fig. 5C). Fig. 5D shows representative tumor samples stained with H&E, EvG and PSR, respectively.

3.3. Analysis of cell nucleus shape

A negative correlation ($R = -0.47$, $p < 0.05$) was found between frequency-independent stiffness μ and elongation of tumor cell nuclei quantified as the mean nucleus aspect ratio (AR) (Fig. 6A). Fluctuations

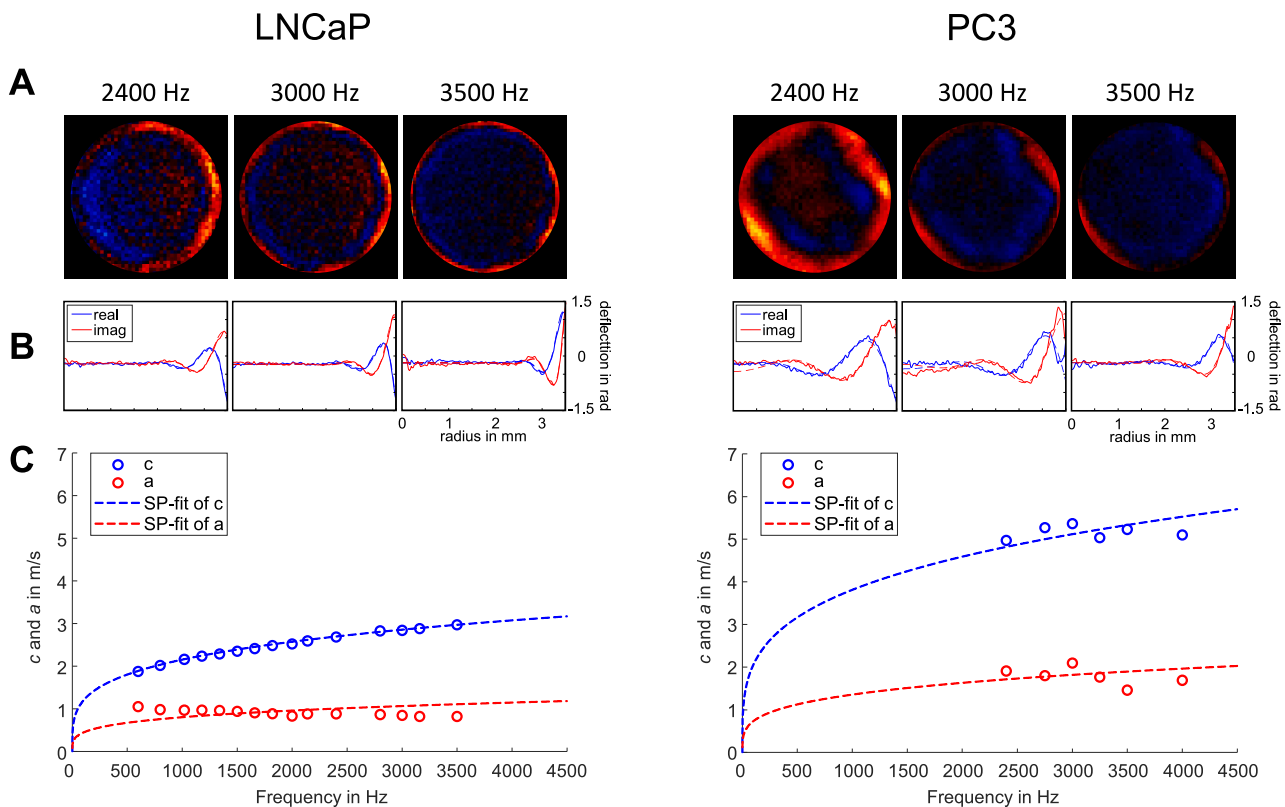


Fig. 2. Experimental wave images and wave number fitting. (A) The real parts of the complex-valued wave images after unwrapping and temporal Fourier transform are shown for three common vibration frequencies applied to an LNCaP tumor (left) and a PC3 tumor (right). (B) Shown below are profile views of the wave images (solid lines) over the radius of the sample tube with the corresponding fits of complex wave number fits (dashed lines) using the analytical model for cylindrical shear waves (see Methods section). (C) Shear wave velocity c and penetration rate a are calculated from the fitted complex wave number. Visual inspection already reveals differences in SWS (stiffness) and penetration rate (inverse attenuation) between the two tumors.

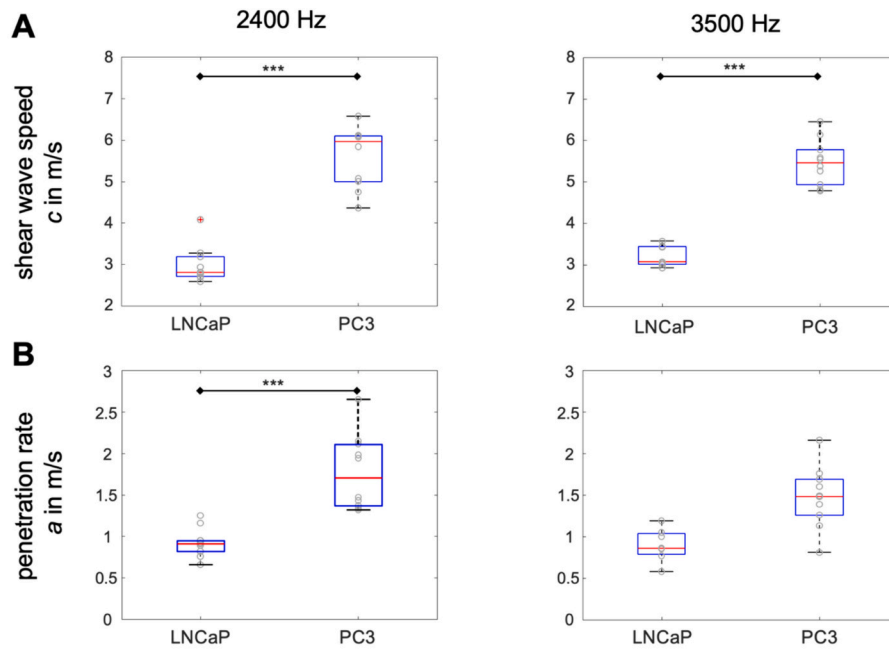


Fig. 3. Box plots of shear wave speed c and penetration rate a for ex vivo MRE of LNCaP and PC3 tumors. (A) SWS is significantly higher for PC3 than for LNCaP tumor types at vibration frequencies of 2400 Hz and 3500 Hz. (B) PR is also higher for PC3 than for LNCaP tumor types. ** $p < 0.005$, *** $p < 0.0005$.

in nuclear aspect ratio also showed a high negative correlation with μ ($R = -0.5$, $p < 0.05$) (Fig. 6B). No significant correlation was found between the mean nuclear AR of PC3 and LNCaP tumor cells and ϕ . The results for the mean AR of LNCaP and PC3 tumors are shown in Fig. 6C. Although more fluid (see Fig. 4C), PC3 tumor cells had significantly lower AR values than LNCaP cells (1.53 ± 0.03 vs. 1.56 ± 0.01 , $p < 0.05$). There was a trend ($p = 0.079$) towards larger nuclear areas in PC3 tumors compared to LNCaP tumors (Fig. 6D).

3.4. Correlation of biophysical imaging parameters with ECM accumulation and nuclear elongation

The three quantitative biophysical structural imaging parameters we determined – stiffness, fluidity, and ADC – were correlated with quantitative measures of ECM components, i.e., elastin and collagen content and nuclear elongation, as characteristics of tumor microenvironment [37] and metastatic potential [24]. In Fig. 7, significant correlations are highlighted in red. The observed increase in collagen and elastin content was positively correlated in both tumor types ($p < 0.05$). Collagen content was positively correlated with stiffness μ ($p < 0.005$). There was also a trend towards such a correlation for elastin ($p = 0.058$). In addition, elastin ($p < 0.05$) and collagen ($p < 0.0005$) content were negatively correlated with water mobility as measured by ADC. The sum of both ECM components also showed a strong negative correlation with ADC ($p < 0.05$). Increasing nuclear elongation, an indicator of cell motility [24], was negatively correlated with stiffness μ ($p < 0.005$) and ADC ($p < 0.0005$).

4. Discussion

The present study shows that xenograft mouse models of human PC3 and LNCaP cell line cancers differ significantly in their biophysical parameters of stiffness, fluidity, and water diffusion. Furthermore, our quantitative histology findings reveal differences in ECM components between the two tumor types, with greater nuclear morphology variance associated with nuclear elongation. In the following, we discuss our results in terms of the relationship between histologically determined changes in the microarchitecture of PC3- and LNCaP-derived cancers,

biophysical properties assessed at a coarser, macroscopic level by ex vivo MRE and DWI, and confounding factors for the determination of tumor stiffness and fluidity.

4.1. Stiffness and ECM accumulation

Collagen metabolism is known to be dysregulated in PCa [38], resulting in increased collagen type I and type III deposition in the ECM [30,39] and higher tumor stiffness [40], independent of tumor size. High elastin expression has been found in many tumors, and elastin crosslinking with other ECM components has implications for tumorigenesis [41]. Quantitative histology revealed significantly higher levels of collagen and elastin in PC3 compared to LNCaP tumors. Consistently, stiffness was also significantly increased in PC3 compared to LNCaP tumors, as shown by the surrogate parameter shear wave speed c – both in the frequency-dependent plot (see Fig. 2) and when c was derived from rheological model parameters (see Fig. 3). This is consistent with a study by Li et al. [42], which showed that collagen is an important determinant of tumor viscoelasticity for a variety of orthotopic breast and pancreatic cancer xenograft models in mice. We also found a positive correlation between collagen and elastin content, and both collagen and elastin fibers have been reported to be involved in processes that promote tumor invasion, metastatic transformation [43], aberrant angiogenesis, and cell proliferation [44]. Considering the positive correlation between Gleason score (aggressiveness) and stiffness reported for patients with PCa in vivo [45], we would expect PC3 tumors to be more aggressive than LNCaP tumors. However, further studies are needed to provide information on tumor growth to prove this hypothesis. This factor was not investigated in our study. This conclusion, based on stiffness as a marker of ECM collagen and elastin accumulation, is supported by the different biology of the two tumor types. PC3-derived tumors are often used as a model for advanced PCa, characterized by increased expression of growth factors and cytokines, mutations in tumor suppressor genes, high metastatic potential, and androgen insensitivity [29]. In contrast, LNCaP tumors are an early-stage model with elevated prostate-specific antigen (PSA) expression, low metastatic potential, and androgen sensitivity, making them amenable to anti-androgen therapy [29]. In addition, it would also be important to

Table 1
Summary of shear wave speed c and penetration ratio α of all LNCaP and PC3 tumor samples for all vibration frequencies applied. Group means are given as median and median absolute deviation (MAD).

LNCaP															
f in Hz	600	800	1020	1180	1340	1500	1660	1820	2000	2140	2400	2800	3000	3140	3500
#	c in m/s														
01	2.05	2.23	2.38	2.48	2.60	2.70	2.76	2.71	2.80	2.87	2.94	3.04	–	–	–
02	2.22	2.27	2.34	2.44	2.61	2.65	2.62	2.59	2.63	2.73	2.82	2.92	2.92	–	–
03	2.40	2.53	2.64	2.75	2.73	2.82	2.89	3.04	3.10	3.10	3.19	3.26	3.36	3.30	3.44
04	2.37	2.54	2.79	2.92	3.41	3.70	3.88	3.96	3.89	3.79	4.08	4.29	–	–	–
05	1.90	2.04	2.19	2.26	2.31	2.38	2.44	2.51	2.55	2.62	2.71	2.86	2.87	2.91	3.00
06	1.97	2.09	2.22	2.32	2.43	2.47	2.55	2.61	2.67	2.73	2.80	2.93	2.97	3.00	3.04
07	1.65	1.85	2.03	2.16	2.22	2.30	2.33	2.47	2.58	2.57	2.77	2.97	3.01	3.10	3.43
08	–	–	–	–	2.97	3.10	3.10	3.16	3.15	3.22	3.28	3.42	3.42	3.51	3.57
09	2.17	2.28	2.38	2.43	2.52	2.53	2.58	2.67	2.67	2.68	2.70	2.80	2.93	2.96	3.07
10	–	–	2.34	2.36	2.33	2.39	2.39	2.39	2.44	2.54	2.59	2.62	2.67	2.78	2.93
Median	2.11	2.25	2.34	2.43	2.56	2.59	2.6	2.64	2.67	2.73	2.81	2.95	2.95	3.00	3.07
(MAD)	(0.20)	(0.18)	(0.16)	(0.16)	(0.25)	(0.29)	(0.30)	(0.30)	(0.28)	(0.26)	(0.27)	(0.29)	(0.17)	(0.18)	(0.21)
#	α in m/s														
01	1.03	0.98	0.92	0.90	0.85	0.87	0.91	1.00	0.90	0.94	0.95	0.95	–	–	–
02	1.09	0.97	0.90	0.88	0.92	0.95	0.92	1.00	0.89	0.90	0.95	0.95	0.99	–	–
03	1.48	1.43	1.34	1.31	1.26	1.17	1.18	1.17	1.15	1.13	1.16	1.09	1.08	1.08	1.05
04	1.09	0.81	0.75	0.68	0.61	0.68	0.73	0.86	0.86	0.79	0.82	0.83	–	–	–
05	1.08	1.01	1.00	1.00	0.99	0.97	0.93	0.91	0.86	0.91	0.91	0.89	0.87	0.85	0.85
06	1.12	1.07	1.07	1.03	1.09	1.04	0.99	0.95	0.94	0.94	0.89	0.87	0.83	0.81	0.86
07	0.79	0.75	0.74	0.73	0.76	0.75	0.72	0.63	0.68	0.64	0.66	0.68	0.66	0.67	0.58
08	–	–	–	–	1.24	1.31	1.30	1.35	1.32	1.27	1.25	1.20	1.21	1.19	1.19
09	1.24	1.12	1.10	1.06	1.04	0.98	0.98	1.01	0.97	0.97	0.92	0.89	0.96	0.98	1.00
10	–	–	0.91	0.89	0.89	0.83	0.79	0.76	0.76	0.77	0.76	0.73	0.74	0.79	0.77
Median	1.09	1.00	0.96	0.95	0.95	0.96	0.93	0.97	0.89	0.92	0.91	0.89	0.92	0.85	0.86
(MAD)	(0.12)	(0.14)	(0.14)	(0.14)	(0.16)	(0.14)	(0.13)	(0.14)	(0.12)	(0.12)	(0.12)	(0.11)	(0.14)	(0.14)	(0.15)

PC3					
f in Hz	2400	2750	3250	3500	4000
#	c in m/s				
01	6.11	5.85	5.72	5.54	6.34
02	5.07	5.12	4.83	4.93	4.92
03	6.57	6.35	6.54	6.45	6.61
04	5.84	5.59	5.25	4.81	5.41
05	6.07	5.84	5.46	5.38	5.08
06	4.36	4.38	4.59	5.77	4.72
07	5.00	5.30	5.06	5.26	5.13
08	4.75	4.73	4.57	4.78	4.75
09	6.09	5.91	5.44	5.58	5.64
10	6.10	6.04	6.13	6.13	5.75
Median (MAD)	5.96 (0.54)	5.72 (0.44)	5.35 (0.45)	5.46 (0.39)	5.27 (0.47)
#	α in m/s				
01	1.98	1.74	1.74	1.60	2.07
02	1.43	1.45	1.46	1.48	1.26
03	2.65	2.20	2.05	2.16	2.26
04	1.34	1.37	1.21	1.13	1.31
05	2.11	1.94	1.84	1.76	1.66
06	1.32	1.28	1.46	0.81	1.40
07	1.94	1.83	1.79	1.49	1.72
08	1.37	1.32	1.30	1.26	1.31
09	2.15	2.06	1.63	1.69	1.62
10	1.47	1.51	1.49	1.39	1.35
Median (MAD)	1.70 (0.35)	1.62 (0.26)	1.56 (0.19)	1.48 (0.24)	1.51 (0.25)

analyze cancer-associated fibroblasts (CAFs) in the future, as they also play a critical role during tumor progression [46] and also in the progression stage [47,48]. CAFs play an important role in the tumor microenvironment (TME), by communicating with PCa cells and modifying their metabolism and drug sensitivity [49]. In the early stage of tumor progression, there is a morphologic change, particularly an overexpression of hyaluronate, fibronectin and collagen, which leads to increased stiffness of the ECM [49–52]. Studies suggest that CAFs alter the arrangement of the reactive stroma and control the motility of PCa cells, thereby creating a tumor-promoting environment [49,53,54].

However, further studies are needed to determine the level of CAFs in PC3 and LNCaP tumors.

Thus, an increase in ECM stiffness in the cancer cell microenvironment provides the basis necessary for tumorigenesis and metastatic spread. Even limited access to this information through macroscopic stiffness measurement of tumor tissue is a valuable step towards improving the diagnosis and prognosis of patients with cancer.

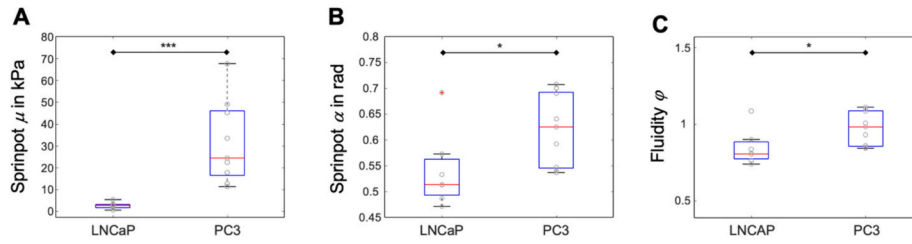


Fig. 4. Box plots for rheological modeling of LNCaP and PC3 tumors. (A) Stiffness μ , (B) structure parameter α of the spring-pot model, and (C) fluidity φ are significantly increased for PC3 tumors. * $p < 0.05$, *** $p < 0.0005$.

Table 2

Spring-pot model-based stiffness μ , structure parameter α , and fluidity φ of all LNCaP and PC3 tumor samples. Group means are given as median and median absolute deviation (MAD).

Spring-pot	LNCaP			PC3		
#	μ inPa	α	φ	μ inPa	α	φ
01	3236.50	0.53	0.84	45,060.93	0.59	0.93
02	3076.73	0.51	0.80	17,693.68	0.63	0.98
03	5382.01	0.47	0.74	67,484.31	0.54	0.84
04	4073.29	0.79	1.24	22,426.59	0.70	1.10
05	2390.77	0.51	0.81	33,496.05	0.54	0.85
06	2744.50	0.51	0.80	11,335.80	0.69	1.08
07	621.32	0.69	1.09	24,350.12	0.55	0.86
08	5936.11	0.49	0.77	12,655.70	0.64	1.01
09	3152.14	0.49	0.76	38,246.41	0.57	0.89
10	1476.00	0.57	0.90	48,933.22	0.71	1.11
Median	3114.43	0.51	0.81	28,923.09	0.61	0.96
(MAD)	(1147.07)	(0.06)	0.10	(13,159.91)	(0.05)	0.09

Table 3

Diffusion-weighted imaging. Summarized are apparent diffusion coefficients (ADC) of all LNCaP and PC3 tumor samples. Group means are given as median and median absolute deviation (MAD).

DWI	LNCaP	PC3
#	ADC in $10^{-3} \text{ mm}^2/\text{s}$	
01	0.87	0.52
02	0.88	0.57
03	0.79	0.47
04	0.86	0.52
05	0.86	0.45
06	0.83	0.56
07	0.84	0.55
08	0.76	0.57
09	1.03	0.55
10	1.02	0.57
Median	0.86	0.55
(MAD)	(0.06)	(0.03)

4.2. Fluidity, stiffness, and cell motility

Despite higher stiffness, PC3 tumors had higher tissue fluidity φ (loss angle of the complex shear modulus) compared with LNCaP tumors (see Fig. 3). The combination of these features indicate the transition of a material from a solid (purely rigid elastic material: $\alpha = 0$, $\varphi = 0$) to a viscous liquid (purely viscous liquid: $\alpha = 1$, $\varphi = \pi/2$) [21] and, in biological tissues, is related to the ability of cells to change their position and relieve deformation stress by dissipation. Motility transition induced by collective cancer cell unjamming can effectively fluidize tissues [24]. Greater elongation and distance of PC3 or LNCaP tumor cells correlates with multicellular motility and higher metastatic potential, which was also found by Gottheil et al. in a study tracking vital tumor cells in breast cancer patients [36]. This is not directly clear for the samples used in this study, but since these parameters are based on cell mechanics at the mesoscale, it is reasonable to assume that they are

independent of the tumor entity. However, the increased fluidity seen in PC3 versus LNCaP cancers contrasts with the more pronounced elongation of tumor cells in LNCaP versus PC3 specimens. The higher fluidity of PC3 tumors could be interpreted in the context of nuclear size. The size of nuclei correlates directly with inverse cell density, and the effective cytoplasmic distance from the nuclear edge to the cell edge increases with nucleus size [24]. Lower cell density in a tissue facilitates cell unjamming, which may be indicated by the observed trend towards larger nuclei in PC3-based tumors. Therefore, despite higher AR values, LNCaP might have less overall liquidity than PC3.

Stiffening and fluidization are characteristics of abnormal changes in a variety of solid cancers. The concomitant increase in stiffness and fluidity in PC3 compared to LNCaP cancers may reveal a viscoelastic signature of higher malignancy, similar to in vivo observations in patients [22].

4.3. Water mobility and ECM accumulation

Complementary to MRE, which determines interactions of cellular and ECM components such as cell-cell adhesion or matrix cross-linking through viscoelasticity, ADC is related to the overall mobility of water molecules and provides information about the microarchitecture at different levels of the structural hierarchy. The ADC is reduced in tissues with tightly packed cells or structures that restrict water movement [55]. Although a lower ADC is often observed in tumors with high cellularity [56], ADC is also sensitive to other histopathological features such as ECM accumulation [57] cell size [58]. The negative correlation between ADC and collagen and elastin content we observed for both tumor types suggests that water movement decreases with increasing ECM content. The lower ADC in PC3 than LNCaP specimens may also be related to the greater amount of elastin and collagen in PC3 tumors. The decrease in ADC due to the alteration of the tumor cell microenvironment caused by the increase in ECM components allows image-based prediction of PCa aggressiveness [59]. The ADC may also be sensitive to the necrotic fraction of tumors, depending on whether the necrotic regions are large enough to be distinguished from viable tissue at the given spatial resolution. Due to the lack of histological evidence in the present study, a significant contribution of necrosis to the increase in ADC can be excluded for both tumor types. This is supported by a recent study in an identical xenograft model where immunohistochemically necrosis was absent in PC3 tumors [60–62].

4.4. The role of cell density, fat cells, and tumor vascularization

In addition to water mobility, cell density also influences stiffness. In biological tissues with high cell density, such as tumors, higher solid stress caused by proliferation in a rigid or fibrotic environment [22] leads to increased stiffness, while at the same time ADC decreases due to the presence of more cell membranes and structures [63]. In contrast to the trend towards lower densities for the cellular components of PC3 tumors, the significantly higher stiffness of PC3 tumors (Fig. 4A), together with significantly increased amounts of collagen and elastin (Fig. 5), indicate a dominant influence of ECM accumulation and thus

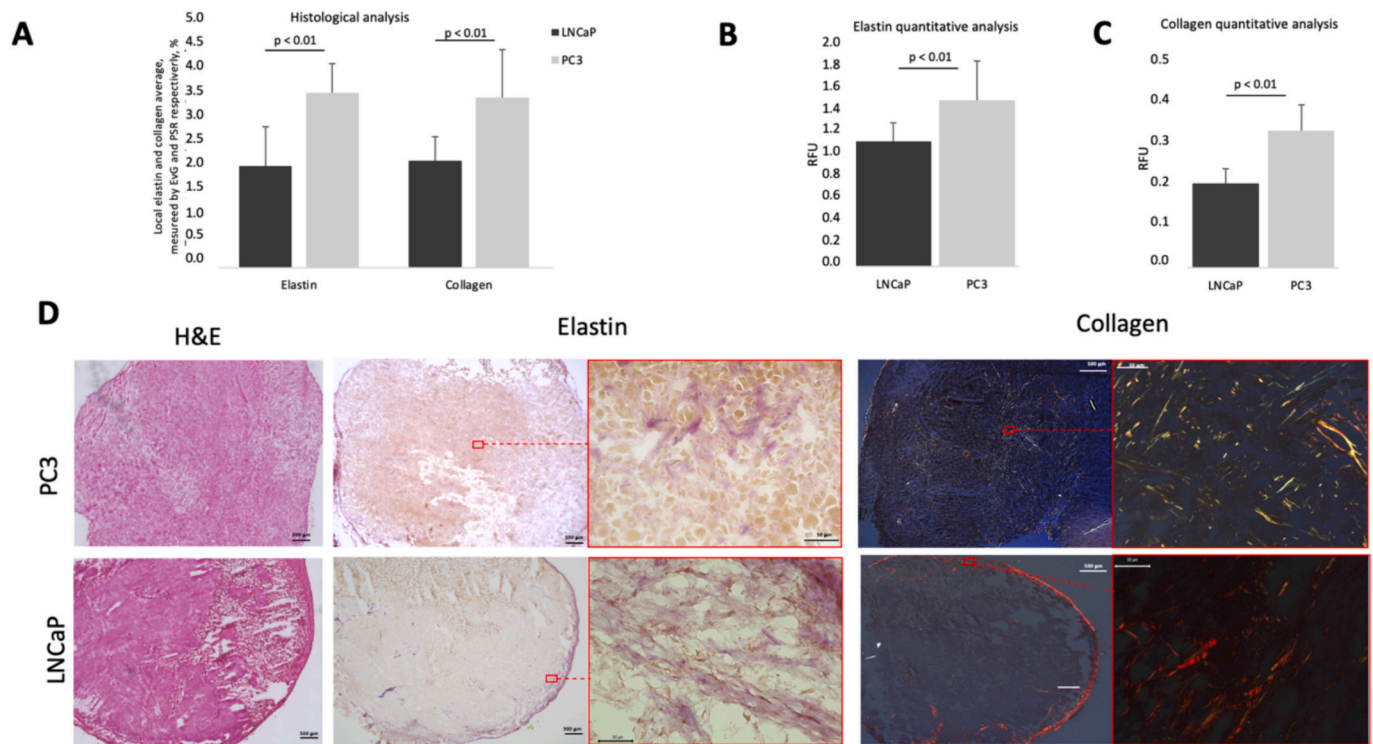


Fig. 5. Histological analysis of elastin and collagen content of LNCaP and PC3 tumors. (A) Results of elastin and collagen analysis in LNCaP ($n = 10$) and PC3 tumors ($n = 10$). The left side shows the percentage of elastin in LNCaP and PC3 tumors. The right side shows the percentage of collagen per tumor. (B) Quantitative results of elastin analysis for LNCaP and PC3. (C) Quantitative results of collagen analysis for LNCaP and PC3. (D) Representative examples of H&E (left), EvG staining (middle) and PSR staining (right) of a PC3 tumor (top) and LNCaP tumor (bottom) with 40 \times magnification of a detail. Purple areas show elastin fibers, yellow areas show cytoplasm. (For interpretation of the references to color in this figure legend, the reader is referred to the web version of this article.)

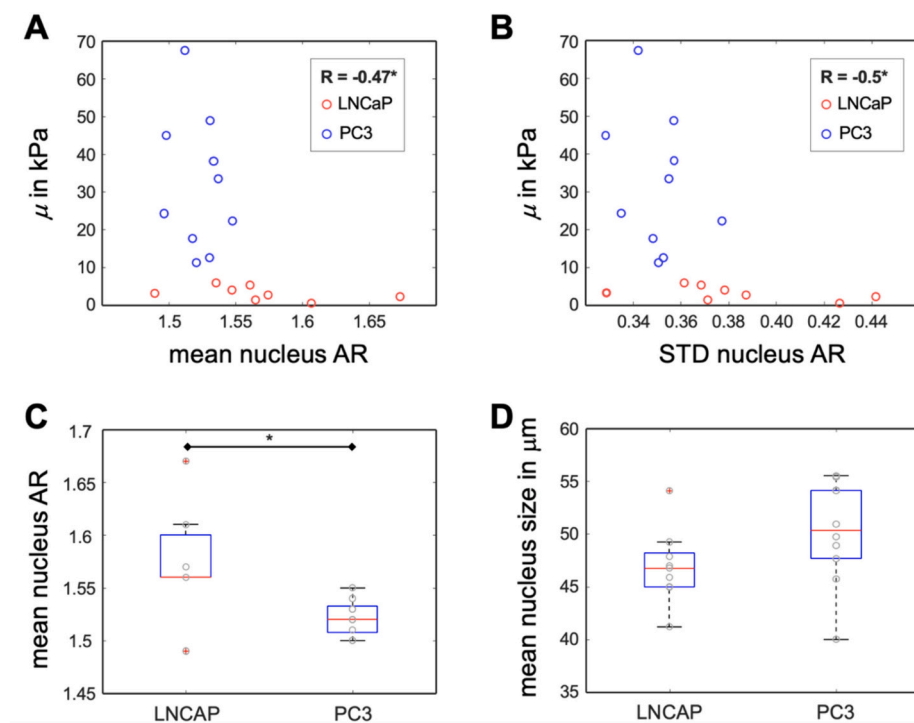


Fig. 6. Results of nuclear shape analysis for LNCaP and PC3 tumors. There is a modest correlation between the decrease in frequency-independent tumor stiffness μ and the increase in mean nuclear AR (elongation) (A) as well as the increase in variance of nuclear morphology (B). Nuclear elongation is significantly higher in LNCaP versus PC3 tumors (C). In addition, there is a trend towards larger nuclear areas in PC3 tumors (D). * $p < 0.05$.

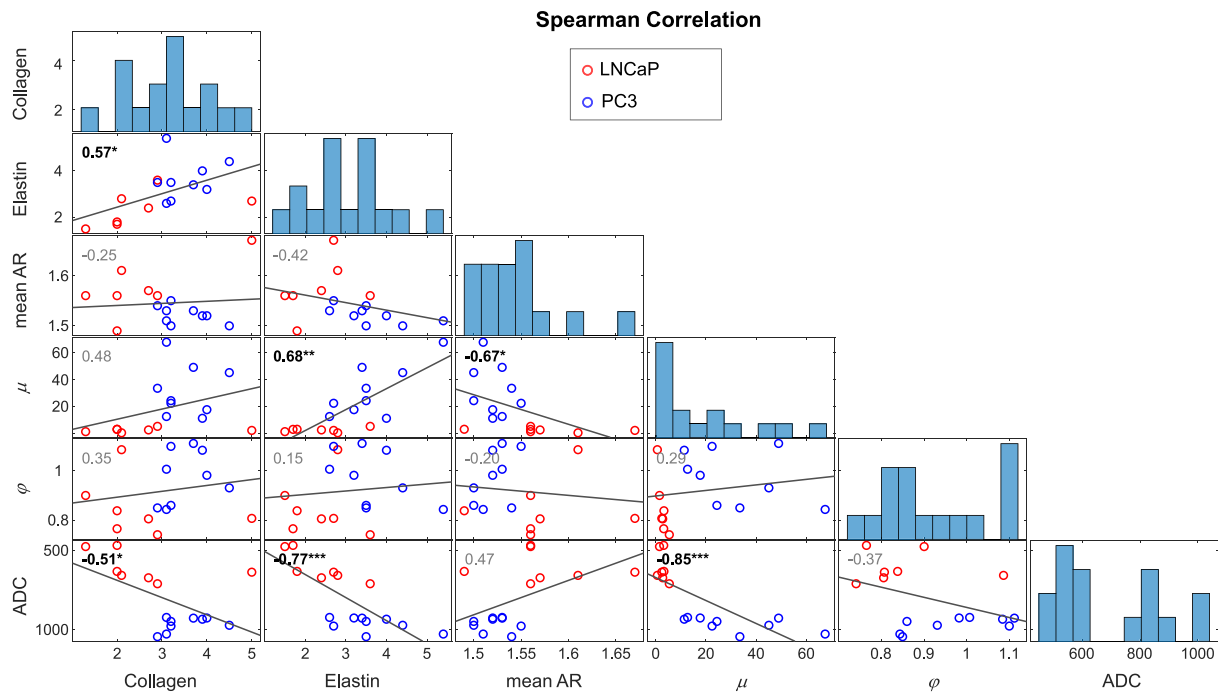


Fig. 7. Correlation of quantitative histological and biophysical imaging parameters. Data distributions are shown as bar graphs on the diagonal. R-values for the respective correlations are given in the upper left corner of the boxes. Mean AR: cell nucleus elongation, μ : spring-pot-based stiffness in kPa, ϕ : fluidity, ADC: apparent diffusion coefficient in $\mu\text{m}^2/\text{s}$. *: $p < 0.05$, **: $p < 0.05$, ***: $p < 0.005$.

increased solid stress in PC3 tumors. Therefore, we argue that the influence of cell density on stiffness is limited in the PCa models investigated in our study. Rather, increases and differences in stiffness can be largely attributed to the amount of collagen and elastin in the tumor ECM.

PCa is known to be a lipid-enriched tumor [64], and there is evidence that the metabolic reprogramming of PCa cells is a hallmark of rapid proliferation and tumor formation [65]. The lipid profile of PCa cells varies with the cell type; however, elevated levels of phospholipids have been observed in prostate LNCaP and PC3 tumor cells [66]. Recently, softening of adipocytes with a concomitant decrease in fluidity has been observed at the onset of their differentiation, during further maturation, and with increasing size of lipid droplet formation [67]. The observed stiffening of tumor tissue and the increase in fluidity could therefore be reduced by the influence of lipid deposition. Histologically, however, we did not observe any deposition of adipocytes. Therefore, potential confounding of results can be considered minor.

In addition, angiogenesis is essential for tumor growth and metastatic spread and is regulated by pro- and anti-angiogenic signals generated by the tumor and stroma [68]. This is where the two cell lines differ. LNCaP xenografts showed a significantly higher microvessel density (see gross appearance of tissue pieces in Fig. 1C) and different vascular morphology along with low Ang-2 and VEGF expression compared with PC3 tumors [69]. The increase in microvessel density in turn is associated with a higher fluid content, which contributes to increased fluidity. Therefore, increased fluidity is not exclusively indicative of greater tumor cell motility; it may also be attributable to pronounced tumor vascularization or other types of fluid accumulation as well as cell proliferation and necrosis [22].

4.5. Limitations

Although the results presented here are encouraging, our study has limitations. First, the number of mice with PC3 and LNCaP tumors was relatively small. This limited separate statistical analysis of the two tumor types. A longitudinal study design with larger groups would allow

to observe the progression of remodeling of cellular and extracellular tumor components during tumorigenesis. A peculiarity of ectopic xenograft models is the subcutaneous growth of tumors outside the target tissue. An orthotopic xenograft model would have been more appropriate to allow tumor cells to grow directly in the prostate and to study changes in the ECM associated with PCa tumorigenesis. However, an orthotopic mouse model is also more stressful for the animals. In particular, the structure and composition of glycosaminoglycans (GAGs) should be investigated in future studies as they may influence both stiffness and fluidity [21]. Additional histological quantification of fat and vascular markers, e.g., antibody staining against vascular endothelial growth factor (VEGF) and lipids or oil red O staining, may unravel the previously neglected influence of these confounders on stiffness in both tumor types. In addition to the limitations, it should be noted that cell motility was not measured directly but inferred from altered cell shapes.

Furthermore, before the MRE findings we obtained in xenograft models can be translated to PCa staging in the clinical settings, they need to be validated in further MRE studies including tissue sampling and determination of biomarkers in patients. Therefore, it is necessary to account for potential confounders of viscoelastic properties that occur in vivo, such as higher perfusion of PCa compared with surrounding tissue [70]. To this end, preclinical experimental methods, in particular elastography for the very stiff PC3 tumors, need to be adapted to the physiological constraints in mouse models.

5. Conclusion

The use of ectopic xenograft models of human PC3 and LNCaP tumor cell lines helps investigators to link quantitative histological and morphological tumor characteristics with structure-sensitive, coarse-grained biophysical imaging parameters. More collagen and elastin in the tumor microenvironment is an indicator of aggressive cancers and contributes to the significantly higher stiffness of PC3 tumors. Increased elongation and spacing of PC3 or LNCaP tumor cells indicates multi-cellular motility. Calculation of the apparent diffusion coefficient

provides complementary information on the structural density of the extracellular matrix of tumor tissues with similar cellularity. This further refines image-based diagnosis and prognosis based on characteristic microscopic tumor features.

Funding

This research was funded by the German Research Foundation (DFG): SFB 1340 - Matrix in Vision, GRK2260 - BIOphysical Quantitative Imaging Towards Clinical Diagnosis (BIOQIC), and FOR5628 - MRE in Cancer.

CRediT authorship contribution statement

Avan Kader: Writing – review & editing, Writing – original draft, Visualization, Validation, Project administration, Methodology, Formal analysis, Data curation, Conceptualization. **Joachim Snellings:** Writing – review & editing, Data curation. **Lisa C. Adams:** Writing – review & editing, Visualization, Data curation. **Pablo Gotthel:** Writing – review & editing, Formal analysis. **Dilyana B. Mangarova:** Writing – review & editing. **Jennifer L. Heyl:** Writing – review & editing. **Jan O. Kaufmann:** Writing – review & editing. **Jana Moeckel:** Writing – review & editing. **Julia Brangsch:** Writing – review & editing. **Timo A. Auer:** Writing – review & editing. **Federico Collettini:** Writing – review & editing. **Frank Sauer:** Writing – review & editing, Formal analysis. **Bernd Hamm:** Writing – review & editing. **Josef Käs:** Writing – review & editing, Conceptualization. **Ingolf Sack:** Writing – review & editing, Conceptualization. **Marcus R. Makowski:** Writing – review & editing, Supervision, Resources, Project administration, Investigation, Funding acquisition, Conceptualization. **Jürgen Braun:** Writing – review & editing, Writing – original draft, Visualization, Supervision, Software, Project administration, Methodology, Funding acquisition, Formal analysis, Conceptualization.

Declaration of competing interest

The authors declare that they have no known competing financial interests or personal relationships that could have appeared to influence the work reported in this paper.

Data availability statement

The datasets generated during and/or analyzed during the current study are available from the corresponding author on reasonable request.

References

- [1] H. Sung, et al., Global Cancer statistics 2020: GLOBOCAN estimates of incidence and mortality worldwide for 36 cancers in 185 countries, *CA Cancer J. Clin.* 71 (3) (2021) 209–249.
- [2] C. Frantz, K.M. Stewart, V.M. Weaver, The extracellular matrix at a glance, *J. Cell Sci.* 123 (Pt 24) (2010) 4195–4200.
- [3] T.R. Cox, The matrix in cancer, *Nat. Rev. Cancer* 21 (4) (2021) 217–238.
- [4] M. Sala, M. Ros, F. Saltel, A complex and Evolutive character: two face aspects of ECM in tumor progression, *Front. Oncol.* 10 (2020) 1620.
- [5] C. Luthold, et al., The extracellular matrix stiffening: a trigger of prostate Cancer progression and castration resistance? *Cancers (Basel)* 14 (12) (2022).
- [6] D.T. Butcher, T. Alliston, V.M. Weaver, A tense situation: forcing tumour progression, *Nat. Rev. Cancer* 9 (2) (2009) 108–122.
- [7] P.J. Russell, et al., Establishing prostate cancer patient derived xenografts: lessons learned from older studies, *Prostate* 75 (6) (2015) 628–636.
- [8] Z. Yuan, et al., Extracellular matrix remodeling in tumor progression and immune escape: from mechanisms to treatments, *Mol. Cancer* 22 (1) (2023) 48.
- [9] K. Hoyt, et al., Tissue elasticity properties as biomarkers for prostate cancer, *Cancer Biomark.* 4 (2011) 213–225.
- [10] D. Hanahan, R.A. Weinberg, The hallmarks of cancer, *Cell* 100 (1) (2000) 57–70.
- [11] A. Palumbo Jr., et al., Extracellular matrix secreted by reactive stroma is a main inducer of pro-tumorigenic features on LNCaP prostate cancer cells, *Cancer Lett.* 321 (1) (2012) 55–64.
- [12] A.W. Partin, High-grade prostatic intraepithelial neoplasia on a prostate biopsy—what does it mean? *Reviews in Urology* 4 (2002) 157–158.
- [13] C. Osorio, et al., Expression of stromal elements of prostatic adenocarcinoma in different Gleason scores, *Acta Cir. Bras.* 34 (10) (2019) e201901005.
- [14] I. Sack, Magnetic resonance elastography from fundamental soft-tissue mechanics to diagnostic imaging, *Nature Reviews Physics* 5 (1) (2022) 25–42.
- [15] M. Reiss-Zimmermann, et al., High resolution imaging of viscoelastic properties of intracranial Tumours by multi-frequency magnetic resonance Elastography, *Clin. Neuroradiol.* 25 (4) (2015) 371–378.
- [16] M. Shahryari, et al., Tomoelastography distinguishes noninvasively between benign and malignant liver lesions, *Cancer Res.* 79 (22) (2019) 5704–5710.
- [17] E. Gultekin, et al., Added value of Tomoelastography for characterization of pancreatic neuroendocrine tumor aggressiveness based on stiffness, *Cancers (Basel)* 13 (20) (2021).
- [18] M. Li, et al., Tomoelastography based on multifrequency MR Elastography for prostate Cancer detection: comparison with multiparametric MRI, *Radiology* 299 (2) (2021) E259.
- [19] R.S. Sahebjavaher, et al., MR elastography and diffusion-weighted imaging of ex vivo prostate cancer: quantitative comparison to histopathology, *NMR Biomed.* 28 (1) (2015) 89–100.
- [20] F. Sauer, et al., Collagen networks determine viscoelastic properties of connective tissues yet do not hinder diffusion of the aqueous solvent, *Soft Matter* 15 (14) (2019) 3055–3064.
- [21] K.J. Streiberger, et al., How tissue fluidity influences brain tumor progression, *Proc. Natl. Acad. Sci. U. S. A.* 117 (1) (2020) 128–134.
- [22] F. Sauer, et al., Changes in tissue fluidity predict tumor aggressiveness in vivo, *Adv Sci (Weinh)* 10 (26) (2023) e2303523.
- [23] T. Fuhs, et al., Rigid tumours contain soft cancer cells, *Nat. Phys.* 18 (12) (2022) 1510–1519.
- [24] P. Gotthel, et al., State of cell unjamming correlates with distant metastasis in cancer patients, *Physical Review X* 13 (3) (2023) 031003.
- [25] M.K. Thomsen, M. Busk, Pre-clinical models to study human prostate Cancer, *Cancers (Basel)* 15 (17) (2023).
- [26] S.I. Park, et al., Pre-clinical mouse models of human prostate cancer and their utility in drug discovery, *Curr Protoc Pharmacol*, Chapter 14: p, Unit 14 (2010) 15.
- [27] M.E. Kaighn, et al., Establishment and characterization of a human prostatic carcinoma cell line (PC-3), *Invest. Urol.* 17 (1) (1979) 16–23.
- [28] J.S. Horoszewicz, et al., LNCaP model of human prostatic carcinoma, *Cancer Res.* 43 (4) (1983) 1809–1818.
- [29] J.K. Rudzinski, et al., The role of the androgen receptor in prostate cancer-induced platelet aggregation and platelet-induced invasion, *J. Thromb. Haemost.* 18 (11) (2020) 2976–2986.
- [30] Y. Wang, et al., Assessment of tumor stiffness with shear wave Elastography in a human prostate Cancer xenograft implantation model, *J. Ultrasound Med.* 36 (5) (2017) 955–963.
- [31] J. Braun, et al., A compact 0.5 T MR elastography device and its application for studying viscoelasticity changes in biological tissues during progressive formalin fixation, *Magn. Reson. Med.* 79 (1) (2018) 470–478.
- [32] H. Tzschatsch, et al., Tomoelastography by multifrequency wave number recovery from time-harmonic propagating shear waves, *Med. Image Anal.* 30 (2016) 1–10.
- [33] Hirsch S, B.J., Sack I., Magnetic Resonance Elastography: Physical Background and Medical Applications. . 2016: Weinheim: Wiley-VCH Verlag GmbH & Co. KGaA.
- [34] A. Bonfanti, et al., Fractional viscoelastic models for power-law materials, *Soft Matter* 16 (26) (2020) 6002–6020.
- [35] K. Garczynska, et al., Effect of post-mortem interval and perfusion on the biophysical properties of ex vivo liver tissue investigated longitudinally by MRE and DWI, *Front. Physiol.* 12 (2021) 696304.
- [36] P. Gotthel, et al., State of cell unjamming correlates with distant metastasis in cancer patients, *Phys. Rev. X* 13 (3) (2023).
- [37] X. He, B. Lee, Y. Jiang, Cell-ECM interactions in tumor invasion, *Adv. Exp. Med. Biol.* 936 (2016) 73–91.
- [38] L.G.R. Calderon, et al., Characterization of collagen fibers (I, III, IV) and elastin of Normal and neoplastic canine prostatic tissues, *Vet Sci* 6 (1) (2019).
- [39] V. Gkretsi, T. Stylianopoulos, Cell adhesion and matrix stiffness: coordinating cancer cell invasion and metastasis, *Front. Oncol.* 8 (2018) 145.
- [40] R.K. Jain, J.D. Martin, T. Stylianopoulos, The role of mechanical forces in tumor growth and therapy, *Annu. Rev. Biomed. Eng.* 16 (2014) 321–346.
- [41] Y. Wang, E.C. Song, M.B. Resnick, Elastin in the tumor microenvironment, *Adv. Exp. Med. Biol.* 1272 (2020) 1–16.
- [42] J. Li, et al., Investigating the contribution of collagen to the tumor biomechanical phenotype with noninvasive magnetic resonance Elastography, *Cancer Res.* 79 (22) (2019) 5874–5883.
- [43] B. Kruslin, M. Ulamec, D. Tomas, Prostate cancer stroma: an important factor in cancer growth and progression, *Bosn. J. Basic Med. Sci.* 15 (2) (2015) 1–8.
- [44] A. Scandolera, et al., The elastin receptor complex: a unique Matricellular receptor with high anti-tumoral potential, *Front. Pharmacol.* 7 (2016) 32.
- [45] S. Li, et al., A feasibility study of MR elastography in the diagnosis of prostate cancer at 3.0T, *Acta Radiol.* 52 (3) (2011) 354–358.
- [46] D. Ohlund, E. Elyada, D. Tuveson, Fibroblast heterogeneity in the cancer wound, *J. Exp. Med.* 211 (8) (2014) 1503–1523.
- [47] F. Mo, et al., Stromal gene expression is predictive for metastatic primary prostate Cancer, *Eur. Urol.* 73 (4) (2018) 524–532.
- [48] M.F. Penet, et al., Structure and function of a prostate Cancer dissemination-permissive extracellular matrix, *Clin. Cancer Res.* 23 (9) (2017) 2245–2254.

- [49] M. Bedeschi, et al., Cancer-associated fibroblast: role in prostate Cancer progression to metastatic disease and therapeutic resistance, *Cells* 12 (5) (2023).
- [50] D. Lavie, et al., Cancer-associated fibroblasts in the single-cell era, *Nat Cancer* 3 (7) (2022) 793–807.
- [51] E. Elyada, et al., Cross-species single-cell analysis of pancreatic ductal adenocarcinoma reveals antigen-presenting Cancer-associated fibroblasts, *Cancer Discov.* 9 (8) (2019) 1102–1123.
- [52] A. Sebastian, et al., Single-cell transcriptomic analysis of tumor-derived fibroblasts and Normal tissue-resident fibroblasts reveals fibroblast heterogeneity in breast Cancer, *Cancers (Basel)* 12 (5) (2020).
- [53] F. Bonollo, et al., The role of Cancer-associated fibroblasts in prostate Cancer tumorigenesis, *Cancers (Basel)* 12 (7) (2020).
- [54] E.V. Nguyen, et al., Proteomic profiling of human prostate Cancer-associated fibroblasts (CAF) reveals LOXL2-dependent regulation of the tumor microenvironment, *Mol. Cell. Proteomics* 18 (7) (2019) 1410–1427.
- [55] D. Le Bihan, et al., MR imaging of intravoxel incoherent motions: application to diffusion and perfusion in neurologic disorders, *Radiology* 161 (2) (1986) 401–407.
- [56] A. Surov, H.J. Meyer, A. Wienke, Correlation between apparent diffusion coefficient (ADC) and cellularity is different in several tumors: a meta-analysis, *Oncotarget* 8 (35) (2017) 59492–59499.
- [57] A. Hauge, et al., Diffusion-weighted MRI-derived ADC values reflect collagen I content in PDX models of uterine cervical cancer, *Oncotarget* 8 (62) (2017) 105682–105691.
- [58] Y. Abe, et al., Modulation of water diffusion by activation-induced neural cell swelling in *Aplysia Californica*, *Sci. Rep.* 7 (1) (2017) 6178.
- [59] D.K. Dwivedi, et al., Stratification of the aggressiveness of prostate cancer using pre-biopsy multiparametric MRI (mpMRI), *NMR Biomed.* 29 (3) (2016) 232–238.
- [60] A. Kader, et al., Iron oxide nanoparticles for visualization of prostate Cancer in MRI, *Cancers (Basel)* 14 (12) (2022).
- [61] A. Kader, et al., Visualization and quantification of the extracellular matrix in prostate Cancer using an elastin specific molecular probe, *Biology (Basel)* 10 (11) (2021).
- [62] A. Kader, et al., Collagen-specific molecular magnetic resonance imaging of prostate Cancer, *Int. J. Mol. Sci.* 24 (1) (2022).
- [63] Patterson, D.M., A.R. Padhani, and D.J. Collins, *Technology insight: water diffusion MRI—a potential new biomarker of response to cancer therapy*. *Nat. Clin. Pract. Oncol.*, 2008. 5(4): p. 220–33.
- [64] Q. Dang, Y.A. Chen, J.T. Hsieh, The dysfunctional lipids in prostate cancer, *Am J Clin Exp Urol* 7 (4) (2019) 273–280.
- [65] X. Zhou, et al., Identification of plasma lipid biomarkers for prostate cancer by lipidomics and bioinformatics, *PloS One* 7 (11) (2012) e48889.
- [66] A. Sorvina, et al., Lipid profiles of prostate cancer cells, *Oncotarget* 9 (85) (2018) 35541–35552.
- [67] S. Abuhattum, et al., Adipose cells and tissues soften with lipid accumulation while in diabetes adipose tissue stiffens, *Sci. Rep.* 12 (1) (2022) 10325.
- [68] L.A. Liotta, P.S. Steeg, W.G. Stetler-Stevenson, Cancer metastasis and angiogenesis: an imbalance of positive and negative regulation, *Cell* 64 (2) (1991) 327–336.
- [69] T. Tesan, et al., Differential expression of angiopoietin-2 and vascular endothelial growth factor in androgen-independent prostate cancer models, *BJU Int.* 102 (8) (2008) 1034–1039.
- [70] T. Franiel, et al., Evaluation of normal prostate tissue, chronic prostatitis, and prostate cancer by quantitative perfusion analysis using a dynamic contrast-enhanced inversion-prepared dual-contrast gradient echo sequence, *Invest. Radiol.* 43 (7) (2008) 481–487.